Journal of Materials Chemistry A

PAPER

View Article Online
View Journal | View Issue

Cite this: J. Mater. Chem. A, 2016, 4, 16073

Stabilizing nickel-rich layered cathode materials by a high-charge cation doping strategy: zirconium-doped $LiNi_{0.6}Co_{0.2}Mn_{0.2}O_2$†

Florian Schipper,‡[a] Mudit Dixit,‡[a] Daniela Kovacheva,[b] Michael Talianker,[c] Ortal Haik,[a] Judith Grinblat,[a] Evan M. Erickson,[a] Chandan Ghanty,[a] Dan T. Major,*[a] Boris Markovsky*[a] and Doron Aurbach[a]

Received 6th August 2016
Accepted 12th September 2016

DOI: 10.1039/c6ta06740a

www.rsc.org/MaterialsA

Ni-rich layered lithiated transition metal oxides $Li[Ni_xCo_yMn_z]O_2$ ($x + y + z = 1$) are the most promising materials for positive electrodes for advanced Li-ion batteries. However, one of the drawbacks of these materials is their low intrinsic stability during prolonged cycling. In this work, we present lattice doping as a strategy to improve the structural stability and voltage fade on prolonged cycling of $LiNi_{0.6}Co_{0.2}Mn_{0.2}O_2$ (NCM-622) doped with zirconium (+4). It was found that $LiNi_{0.56}Zr_{0.04}Co_{0.2}Mn_{0.2}O_2$ is stable upon galvanostatic cycling, in contrast to the undoped material, which undergoes partial structural layered-to-spinel transformation during cycling. The current study provides sub-nanoscale insight into the role of Zr^{4+} doping on such a transformation in Ni-rich $Li[Ni_xCo_yMn_z]O_2$ materials by adopting a combined experimental and first-principles theory approach. A possible mechanism for a Ni-mediated layered-to-spinel transformation in Ni-rich NCMs is also proposed.

1. Introduction

Current applications of Li-ion batteries (LIBs) range from portable electronic devices to electric vehicles (EVs) due to the excellent performance of these batteries in terms of power and energy density.[1–3] Numerous promising positive electrodes (cathodes) for LIBs are based on lithiated transition metal oxides of the general formula $Li[Ni_xCo_yMn_z]O_2$ (*i.e.* NCM). Within the NCM-family of materials, Ni-rich variants (*i.e.* $x > 0.5$) have emerged in recent years as an alternative to the mature $LiCoO_2$. In spite of tremendous promise, these materials still face various challenges in practical commercialization for EVs. Key concerns are how to effectively stabilize the structure of these materials during prolonged charge/discharge cycling, increase their electrochemical activity and rate capability, reduce the heat evolution of the electrodes in a charged state, and lessen capacity fading. One of the prevailing approaches to tackle these concerns is doping $Li[Ni_xCo_yMn_z]O_2$ with cations.[4] In this respect, several mono- and multi-valent doping cations, like Ag^+, Na^+, Co^{2+}, Cu^{2+}, Mg^{2+}, Zn^{2+}, Ba^{2+}, Al^{3+}, Fe^{3+}, Cr^{3+}, Ga^{3+}, Zr^{4+}, Ti^{4+} *etc.*, as well as non-metallic ions (boron, fluorine), were explored for layered, spinel, and olivine structure cathode materials.[4–10] In spite of much effort in identifying optimal dopants, doping electrode materials with various cations and anions still remains an important and challenging methodology that can significantly improve Li^+ intercalation/deintercalation characteristics.[9,11]

In order to improve doping of layered oxide cathodes, a deep atomic-level understanding of the effect of impurity on the host material is essential. Recently, Manthiram *et al.*,[12] demonstrated that the segregation of dopants M = Cr, Fe, and Ga to the surface in the doped high-voltage spinel $LiMn_{1.5}Ni_{0.5-x}M_xO_4$ decreased the unwanted surface electrode/solution reactions, suppressed the formation of a solid electrolyte interface (SEI) layer and improved the cycle life at elevated temperatures. These authors also suggested that doping reduces the cationic ordering and thus enhances the rate capability of the electrodes due to an increase in the electronic and Li^+-ion conductivities. Kim and Amine proposed that doping with cations like Ti^{4+} suppresses the migration of Ni^{2+} in the Li layer.[13,14] Guilmard *et al.* performed extensive studies on $Li_xNi_{0.89}Al_{0.16}O_2$ and $Li_xNi_{0.7}Co_{0.15}Al_{0.15}O_2$, and proposed a possible Al^{3+} migration to tetrahedral lattice-sites, thereby suppressing layered-to-spinel transformation.[15,16] In a recent study,[17] we demonstrated that minute Al-doping in $LiNi_{0.5}Co_{0.2}Mn_{0.3}O_2$ reduces capacity fading of the Al-doped electrodes upon cycling, reduces aging of the cells in a charged state (4.3 V) at 60 °C, and produces a more

[a]Department of Chemistry, The Lise Meitner-Minerva Center of Computational Quantum Chemistry, Bar-Ilan University, Ramat-Gan 52900, Israel. E-mail: markovskyboris22@gmail.com; majort@biu.ac.il; Fax: +972 3 738 40 53; Tel: +972 3 531 88 32; +972 3 531 73 92

[b]Institute of General and Inorganic Chemistry, Bulgarian Academy of Sciences, Sofia 1113, Bulgaria

[c]Department of Materials Engineering, Ben-Gurion University of the Negev, Beer-Sheva 84105, Israel

† Electronic supplementary information (ESI) available. See DOI: 10.1039/c6ta06740a

‡ These authors contributed equally to this work.

stable mean voltage behavior. These favorable attributes were ascribed to the chemical and structural modifications of the electrode/solution interface. Recently, the improvements in the performance of cathode materials were achieved by surface fluorination and by the formation of core–shell structures.[18,19]

A particularly promising dopant for NCM is Zr, although its effect is still in dispute in the literature. There are several papers that demonstrate, for instance, superior cycling performance of the doped Ni-rich material $LiNi_{0.8}Co_{0.18}Zr_{0.02}O_2$, compared to the undoped one, especially when the electrodes were charged to higher cut-off potentials.[20] Sun *et al.* demonstrated superior performance of Zr-doped $LiNi_{0.45}Co_{0.1}Mn_{0.45}O_2$ and supported the hypothesis of suppression of Ni^{2+} migration on high-valent cation doping.[21] An increase in the Li diffusion coefficient on Zr doping in $LiNi_{0.33}Co_{0.33}Mn_{0.33}O_2$ has also been observed.[22] It was suggested that the Zr^{4+} dopant ion can act as a structural focal point that decreases the cationic mixing and helps maintain the original hexagonal structure during the Li^+ extraction–insertion processes.[20] Majumder *et al.*[23] proposed that Zr^{4+} ions can occupy lithium sites in $LiNi_{0.8}Co_{0.15}Zr_{0.05}O_2$ and behave as supporting "pillars" that minimize the local constriction of the lithium-ion paths, hence stabilizing the layered structure and enhancing the cycling performance of doped electrodes.

Despite the considerable research of the above materials, an atomic level understanding of the effect of dopants is still limited. Yet, this information is essential for the rational design of new and efficient positive electrode materials for LIBs. In the current paper, we adopt a combined experimental and computational electrochemical approach to pinpoint the role of Zr^{4+} in doped $LiNi_{0.6}Co_{0.2}Mn_{0.2}O_2$. We synthesized undoped $LiNi_{0.6}Co_{0.2}Mn_{0.2}O_2$ and Zr-doped $LiNi_{0.56}Zr_{0.04}Co_{0.2}Mn_{0.2}O_2$ materials using a self-combustion reaction, and studied electrochemical kinetics, surface film (R_{sf}) and charge-transfer (R_{ct}) resistances, and discharge capacities during cycling. We also performed structural analysis during cycling using nano-beam electron diffraction patterns to determine whether a phase-transition occurred or not. To better understand the properties of these novel cathode materials and the mechanism of phase transformations, we compute voltage profiles, material stabilities, and Li-ion diffusion profiles using density functional theory (DFT). This paper is organized as follows: firstly, we characterize the undoped $LiNi_{0.6}Co_{0.2}Mn_{0.2}O_2$ and Zr-doped $LiNi_{0.56}Zr_{0.04}Co_{0.2}Mn_{0.2}O_2$ materials, describe the thermodynamic substitution preference for the Zr^{4+} dopant and the oxidation states of the transition metals; secondly, the electrochemical behavior of undoped and Zr-doped materials is presented along with structural analysis of the cycled electrodes in connection with layered-to-spinel transformation of the above materials studied experimentally by electron diffraction and by computational diffusion paths of Ni^{2+} ions.

2. Computational methods

The Vienna *ab initio* simulation package[24–26] (VASP) was employed to perform DFT electronic structure calculations with spin polarization and antiferromagnetic spin ordering. The generalized gradient approximation (GGA) with the PBE[27] exchange–correlation functional was used with plane-wave projector augmented wave[28] (PAW) based pseudo-potentials. The kinetic energy cutoff was set to 520 eV. To find the relaxed lattice parameters, the volume of the unit cell was optimized and the geometries considered minimized when the maximum force was found to be less than 0.01 eV per atom. The calculation setup was made with 5×4 supercells with 60 formula units of the $R\bar{3}m$ space group with an α-$NaFeO_2$ type structure. Due to the very large super-cells (240 atoms), the calculations were performed using gamma k-point only. To perform GGA+U calculations, U values were selected based on previous studies[29–31] on a similar class of materials. In particular, we employed $U = 5.96$, 5.00 and 5.10 eV for Ni, Co and Mn, respectively. To incorporate dispersion effects, we employed the optPBE-vdW method as implemented in the VASP code.[33,34]

The preference for substitution of Zr at different cation sites in NCM-622 was computed using the substitution energy, which is defined by the following equations:

$$E_{\text{subs-Ni}} = \frac{1}{3}\left[\left\{E_{Li_{60}Ni_{33}Zr_3Co_{12}Mn_{12}O_{120}} + 3E_{LiNiO_2}\right\} - \left\{E_{Li_{60}Ni_{36}Co_{12}Mn_{12}O_{120}} + 3E_{Li} + 3E_{ZrO_2}\right\}\right] \quad (1)$$

$$E_{\text{subs-Co}} = \frac{1}{3}\left[\left\{E_{Li_{60}Ni_{36}Zr_3Co_9Mn_{12}O_{120}} + 3E_{LiCoO_2}\right\} - \left\{E_{Li_{60}Ni_{36}Co_{12}Mn_{12}O_{120}} + 3E_{Li} + 3E_{ZrO_2}\right\}\right] \quad (2)$$

$$E_{\text{subs-Mn}} = \frac{1}{3}\left[\left\{E_{Li_{60}Ni_{36}Zr_3Co_{12}Mn_9O_{120}} + 3E_{LiMnO_2}\right\} - \left\{E_{Li_{60}Ni_{36}Co_{12}Mn_{12}O_{120}} + 3E_{Li} + 3E_{ZrO_2}\right\}\right] \quad (3)$$

where E represents the total energies of corresponding systems, E_{Li} represents the total energy of bulk lithium metal, and E_{ZrO_2} is the total energy of bulk monoclinic ZrO_2. Bulk $LiCoO_2$, $LiNiO_2$ and $LiMnO_2$ are taken as the reference states for Ni, Co and Mn.

Average intercalation potentials were computed using the following equation:

$$V = \left\{\frac{E(Li_{x+dx}NCM) - E(Li_xNCM)}{dx} - E(Li_{bcc})\right\} \quad (4)$$

where $E(Li_{x+dx}NCM)$ and $E(Li_xNCM)$ represent the total energy per formula unit of the system before and after lithium de-intercalation. Various Li configurations were taken into consideration, and we selected the most stable structure for calculating the de-intercalation voltage profiles. Because of computational limitations, a slightly higher concentration of Zr was adopted for *in silico* doped materials ($LiNi_{0.55}Co_{0.2}Mn_{0.2}Zr_{0.05}O_2$) compared to experimental materials ($LiNi_{0.56}Co_{0.2}Mn_{0.2}Zr_{0.04}O_2$).

The Nudged elastic band (NEB)[35] method was used to study cation migration with 400 eV kinetic energy cutoff. For NEB calculations, the lattice parameters for defect structures were fixed at the relaxed lattice parameters obtained using PBE. All the NEB calculations were performed using PBE (without U), as PBE+U often results in mixing of the diffusion barrier with a charge transfer barrier.[36] The dispersion corrections were not

included in the NEB calculations as these calculations are performed close to the fully delithiated level.

3. Results and discussion

3.1 Morphological and structural characterization

3.1.1. Experimental characterization. A typical morphology image measured by SEM of Zr-doped $LiZr_{0.04}Ni_{0.56}Co_{0.2}Mn_{0.2}O_2$ (annealed at 900 °C, 1 h) is shown in Fig. S1.† The particle size ranges from 100 to 500 nm, they are faceted and partly form agglomerates. In this figure, we also present the energy-dispersive analysis spectrum (EDAS) of the material, demonstrating distinctive peaks of Ni, Co, Mn, and Zr. The ratio (atomic percentage) of the elements was found to be 55.5 : 19.8 : 20 : 4.5 close to the desired one from the self-combustion reaction (SCR) (see the Experimental section in the ESI†).

Fig. S2† presents XRD patterns of $LiNi_{0.6}Co_{0.2}Mn_{0.2}O_2$ thermally treated for 1 h at different temperatures, as indicated. The effect of increasing the annealing temperature on the evolution of the layered structure towards separation of transition metal (TM) ions and Li ions into their respective planes is clearly seen. Rietveld analysis revealed, however, that materials obtained after heat treatment at 600, 700 and 800 °C showed a high level of cationic mixing between the Li and 3d-metal layers. For example, the presence of 3d metal ions in the Li layer was found to be as high as 0.25 for the NCM-622 material heated at 700 °C. A satisfactory cationic ordering for the layered materials is obtained only after heat treatment at 900 °C. The mean crystallite size of both materials shows a slight increase within the temperature range of 400–700 °C from 8–9 nm to 15–16 nm. A sharp increase in the crystallite size occurs during heating at 900 °C, where the mean crystallite size increases to 80 nm for the undoped and 105 nm for the Zr-doped samples. The results of Rietveld refinement of the crystal structure of $LiNi_{0.6}Co_{0.2}Mn_{0.2}O_2$ are shown in Table 1.

Synthesis of the Zr-doped compound by SCR resulted in the formation of $LiNi_{0.56}Zr_{0.04}Co_{0.2}Mn_{0.2}O_2$ (dominant phase) and a minor amount of a secondary phase. The dominant phase is a layered material with a $LiNiO_2$ type structure, while the second phase in the sample is Li_2ZrO_3, which is present in a very small amount. The structure of Li_2ZrO_3 is built of layers of octahedrally coordinated metal cations. Contrary to the layered $LiNiO_2$ type structure, where Li and TM-cations are separated into two adjacent layers, in Li_2ZrO_3 the layers perpendicular to the *c*-axis are identical, with Li and Zr ions present in a ratio of 2 : 1. The mass fraction of the Li_2ZrO_3 phase is found to be around 2.5%, which means that the atomic fraction of zirconium in the layered type structure is about 0.04, which is in agreement with the results published by Luo and Dahn.[32] An additional indication that Zr is present in the crystal structure of the layered phase is the greater unit cell parameters of the doped sample compared to the undoped one.

Determining the distribution of Zr between lithium (3b) and 3d-metal (3a) sites on the basis of the XRD pattern is a difficult task, since the quantity of Zr in the structure is minute. Refining Li, Ni and Zr quantities in both layers, as free (even constrained) parameters, resulted in very high standard deviations for the corresponding occupancies. Hence, we performed some refinement with different fixed distributions of Ni over the two positions, allowing Li and Zr occupancies to vary in a constrained manner to fill both cation positions. In this case, the reliability factor, R_{Bragg}, was the indicator for the fit. Fig. S3† represents the relationship between R_{Bragg} and the amount of Ni in the Li layer. As can be seen from this figure, the minimal value for R_{Bragg} is obtained with zero occupancy of Ni in the 3b position. The crystal structure parameters for the best fit are presented in Table 1b. We may conclude that the increase in the unit cell parameters upon Zr substitution is mainly due to an increase in the metal–oxygen distances within the lithium layer, and this correlates well with DFT calculations presented below.

Table 1 Crystal structure data for (a) $LiNi_{0.6}Co_{0.2}Mn_{0.2}O_2$, $R_{wp} = 9.03$, GOF = 1.32, $R_{Bragg} = 2.52$. SG. $R\bar{3}m$, $a = 2.8703(1)$ Å, $c = 14.2134(4)$ Å. (b) $LiNi_{0.56}Zr_{0.04}Co_{0.2}Mn_{0.2}O_2$, $R_{wp} = 10.4$, GOF = 2.685, $R_{Bragg} = 4.29$. SG. $R\bar{3}m$, $a = 2.8709(1)$ Å, $c = 14.2264(4)$ Å

(a) $LiNi_{0.6}Co_{0.2}Mn_{0.2}O_2$[a]

Atom	Site	*x*	*y*	*z*	O_{cc}	B_{izo}
Li	3b	0	0	1/2	0.944(4)	1.3(2)
Ni	3b				0.056(4)	1.3(2)
Ni	3a	0	0	0	0.543(3)	0.97(4)
Co	3a				0.2 fixed	0.97(4)
Mn	3a				0.2 fixed	0.97(4)
Li	3a				0.056(3)	0.97(4)
O	6c	0	0	0.2581(3)	2	1.37(5)

(b) $LiNi_{0.56}Zr_{0.04}Co_{0.2}Mn_{0.2}O_2$[b]

Atom	Site	*x*	*y*	*z*	O_{cc}	$B_{overall}$
Li	3b	0	0	1/2	0.982(1)	2.28(4)
Zr	3b				0.018(1)	2.28(4)
Ni	3a	0	0	0	0.55 fixed	2.28(4)
Co	3a				0.2 fixed	2.28(4)
Mn	3a				0.2 fixed	2.28(4)
Li	3a				0.028(1)	2.28(4)
Zr	3a				0.022(1)	2.28(4)
O	6c	0	0	0.2592(2)	2	2.28(4)

[a] 3b-O distance 2.110(2) Å, 3a-O distance 1.969(2) Å. [b] 3b-O distance 2.117(2) Å, 3a-O distance 1.965(2) Å.

3.1.2. Computational characterization. Lithiated layered oxide electrode materials based on Ni, Co, and Mn, are shown to have limited ordering due to the difference in oxidation states of each ion. It was suggested previously that such ordering is driven by electrostatic interactions,[37] and many authors have proposed a $(\sqrt{3} \times \sqrt{3})$R30 type of ordering in the above class of materials.[38–42] Recently we proposed a multi-scale approach to predict low-energy cationic ordering in layered oxides based on prescreening of various $\sqrt{3}$-ordering structures with classical atomistic simulations, followed by DFT rescoring of the lowest energy structures.[43] We adopted this funneled approach to predict the most stable structure with optimal cationic ordering (Fig. 1).

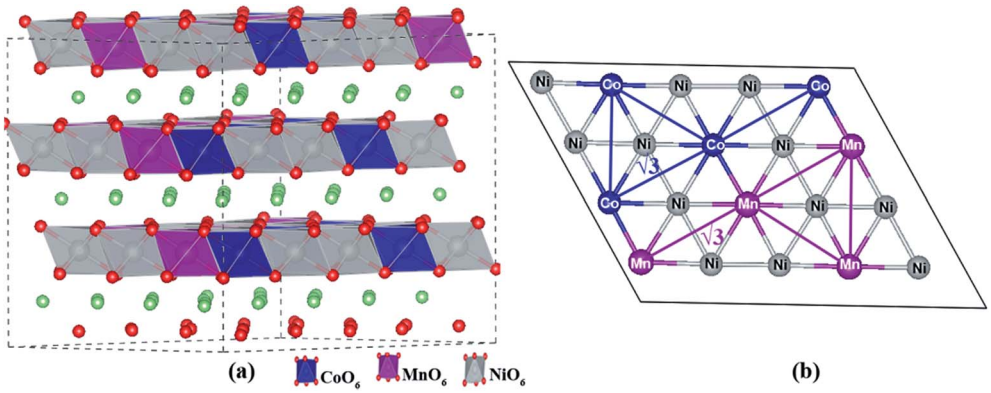

Fig. 1 (a) The supercell of $LiNi_{0.6}Co_{0.2}Mn_{0.2}O_2$, in which Li atoms are marked in green; (b) most preferred cation ordering.

Subsequently, we turned our attention to the prediction of the preferred Zr-doping site. Fig. S4† shows the most preferred Zr substitution positions, whereupon it replaces Ni, Co or Mn. Based on the computed substitution energies, the thermodynamic substitution preference for Zr^{4+} follows the order Ni ($E_{subs} = -1.63$ eV per dopant, TM Layer) > Co ($E_{subs} = -1.62$ eV per dopant) > Ni ($E_{subs} = -1.36$ eV per dopant, Li Layer) > Mn ($E_{subs} = -1.18$ eV per dopant). As discussed in the previous section, EDAS results confirm that Zr is doped preferentially at Ni-sites. We note that the substitution energies are negative for substitution of Ni by Zr in both TM and Li layers. Furthermore, results of Reitveld refinement also suggested that Zr is present in both TM and Li layers.

Table 2 presents the calculated lattice parameters of Li_x-$Ni_{0.6}Co_{0.2}Mn_{0.2}O_2$ ($x = 1$, 0). We obtain reasonable agreement between the calculated and experimental parameters corresponding to the fully intercalated state ($x = 1$). For the fully delithiated material ($x = 0$), the c lattice parameters are higher than expected[44,45] because of the inability of the PBE functional to account for dispersion interactions. As noted recently,[43,46] dispersion becomes important in the low lithiation limit, and inclusion of dispersion results in a characteristic dip in the computed c lattice parameters at $x < 0.50$ (Fig. S5†). Inspection of the parameters for $Ni_{0.56}Co_{0.2}Mn_{0.2}Zr_{0.04}O_2$ shows clearly that both a and c lattice parameters increase on Zr doping. The increase in the c lattice parameter can be attributed to the greater Zr–O average distance (2.11 Å) compared to the Ni–O average distance (2.06 Å) at the same octahedral site. A slight increase in the a lattice parameters on Zr doping was also found. This latter increase is irrespective of the positions of Zr in the TM or Li layer.

The dispersion-corrected PBE results clearly demonstrate that from $x = 1.00$ to $x = 0.00$ the net change in the c lattice parameter is lower for the Zr-doped (in the Li layer) material than for the undoped material. Such a low overall change in the c lattice parameter on Zr doping in the Li layer indicates the suggested "pillar" effect of Zr. Visual inspection of the fully delithiated structure of the Zr-doped (in the TM layer) material reveals that the Zr atoms have moved significantly above the TM plane (for both GGA and dispersion-corrected GGA) (Fig. S6†), suggesting that Zr has some interlayer interaction with the oxygen atoms.

3.2 Electronic structure characterization of undoped and Zr-doped materials

The calculated magnetic moments and projected density of states (PDOS) for $LiNi_{0.6}Co_{0.2}Mn_{0.2}O_2$ and $LiNi_{0.55}Co_{0.2}Mn_{0.2}$-$Zr_{0.05}O_2$ suggest that Ni exists in two different formal oxidation states, Ni^{2+} and Ni^{3+} (Fig. 2). Careful analysis of the PDOS (Fig. 2a, b and S7†) suggests that Ni^{2+} and Ni^{3+} have electronic configurations corresponding to $t_{2g}^6(|\downarrow\uparrow|\downarrow\uparrow|\downarrow\uparrow|)$ $e_g^2(|\ \uparrow|\ \uparrow|)$ and $t_{2g}^6(|\downarrow\uparrow|\downarrow\uparrow|\downarrow\uparrow|)$ $e_g^1(|\ \uparrow|\ |)$, respectively. As expected, due to the greater number of unpaired electrons in Ni^{2+} than in Ni^{3+}, Ni^{2+} has greater exchange splitting. The absence of exchange splitting and magnetic moment on Co ions suggests a +3

Table 2 Calculated a and c lattice parameters (Å) for undoped and Zr-doped NCM-622 using the PBE functional

	a	c	a	c	a	c
	$LiNi_{0.6}Co_{0.2}Mn_{0.2}O_2$		$LiNi_{0.55}Co_{0.2}Mn_{0.2}Zr_{0.05}O_2$		Exp.[c]	
$x = 1.00$	2.89	14.25	2.90[a] 2.90[b]	14.33[a] 14.28[b]	2.87(2.87)	14.21(14.22)
$x = 0.0$	2.84	14.99	2.86[a] 2.83[b]	14.65[a] 14.59[b]		

[a] Zr doped in the TM layer. [b] Zr doped in the Li layer. [c] The experimental values correspond to $LiNi_{0.56}Co_{0.2}Mn_{0.2}Zr_{0.04}O_2$ and the values in parenthesis are for Zr-doped NCM-622.

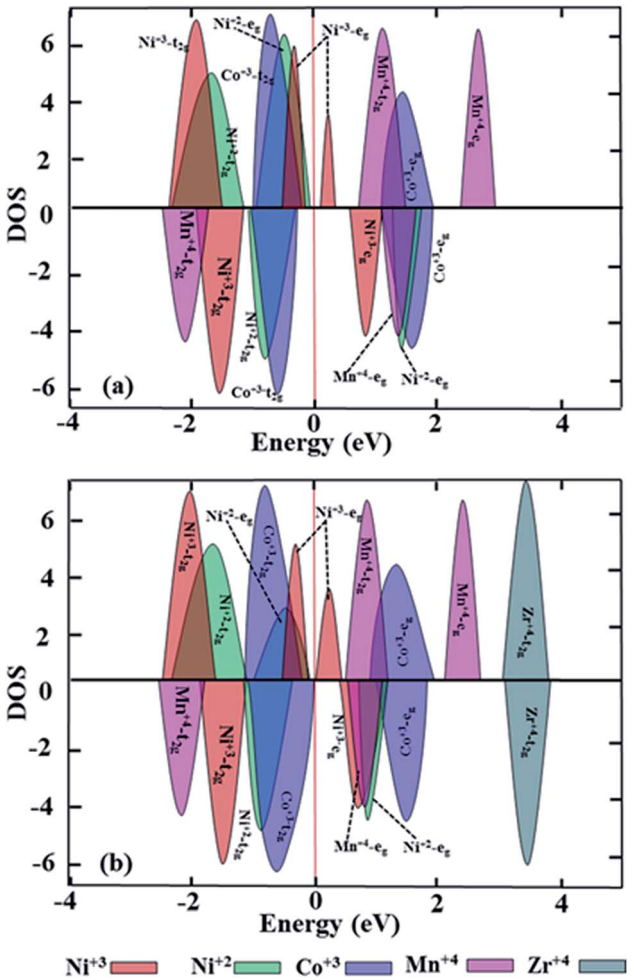

Fig. 2 Schematic projected density of states (PDOS) for (a) $LiNi_{0.6}Co_{0.2}Mn_{0.2}O_2$ and (b) $LiNi_{0.55}Co_{0.2}Mn_{0.2}Zr_{0.05}O_2$ materials using PBE.

valence state and an electronic configuration of $t_{2g}^6(|\downarrow\uparrow|\downarrow\uparrow|\downarrow\uparrow|)\ e_g^0(|\ |\ |)$. In both doped and undoped materials the valence band maximum consists of Ni (Ni^{2+}-e_g and Ni^{3+}-e_g) and Co (Co^{3+}-t_{2g}) states, whereas the conduction band minimum (CBM) primarily consists of Ni^{3+}-e_g states. The spin-singly occupied t_{2g} states of Mn and a magnetic moment higher than 2 μB suggest a half-filled t_{2g} state and a +4 valence state, corresponding to a $t_{2g}^3(|\downarrow\ |\downarrow\ |\downarrow\ |)\ e_g^0(|\ |\ |)$ electronic configuration. The existence of mainly Ni states near the Fermi level suggests a primary role of Ni in the electrochemical activity of NCM-622. Noticeably on Zr doping the band gap of NCM-622 vanishes due to broadening of the Ni and Co states. The broadening appears due to excess electrons donated by Zr^{4+} when compared to Ni^{2+}.

In Fig. 3 we present oxidation states for the transition metals estimated based on the calculated magnetic moments and PDOS. We note that upon Zr-substitution at Ni sites, the number of Ni^{2+} ions increases while the number of Ni^{3+} ions decreases to compensate for the excess positive charge originating from the aliovalent Zr^{4+} dopant. In the radial pair distribution function of the pristine material (Fig. S8†), the existence of two peaks in g_{Ni-O} and a peak near 1.95 Å confirms the presence of a Ni^{3+} Jahn–Teller distortion. We also note that in the Zr-doped material this g_{Ni-O} peak is lowered, providing evidence that the amount of Ni^{3+} ions is indeed reduced on Zr doping. The slight increase in the *a* lattice parameters on Zr doping mentioned above could be rationalized based on this increase in the number of Ni^{2+} ions (ionic radius 0.69 Å) and decrease in Ni^{3+} ions (ionic radius 0.56 Å) on Zr doping. Zr substitution at Mn^{4+} sites does not result in a change in the number of Ni^{2+} and Ni^{3+} ions, as expected due to the isovalent nature of the substitution. On Zr substitution at Co^{3+} sites, the number of Ni^{2+} ions is increased while the number of Ni^{3+} ions decreases to compensate for the extra positive charge from Zr^{4+}. Clearly, Ni is the main redox active ion, which serves as a charge modulator. Hence, the increase in the specific capacity on Zr doping could be attributed to the higher ratio of Ni^{2+} (two redox electrons/ion) to Ni^{3+} (one redox electron/ion) in the doped material.

3.3 Electrochemical redox behavior of electrodes comprising $LiNi_{0.6}Co_{0.2}Mn_{0.2}O_2$ undoped and Zr-doped materials

The positive effects of Zr-doping are reflected in the improved electrochemical performance of electrodes comprising Zr^{4+} doped materials, as presented in the following section, in which we demonstrate more stable cycling behavior, faster kinetics, lower impedance and voltage fade of the doped samples.

3.3.1. Computational characterization. The average intercalation voltage is one of the primary properties of any LIB cathode material. The voltage profiles calculated using PBE (shifted) and the dispersion corrected PBE (shifted) show good agreement with the experimental data (Fig. 4). As shown in our recent study on NCM-523,[43] the PBE+U method is not able to reproduce the voltage trends of NCM materials. We suggest that the inability of the PBE+U method in computing the voltages is not a failure of the PBE+U method itself but it is mainly due to change in electron correlation of NCM-622 as a function of Li de-intercalation and due to the requirement of different *U* values for cations at different states of charge.[43]

3.3.2. Experimental characterization. First, we established that electrodes made from the Zr-doped material demonstrate advanced electrochemical performance compared to their undoped counterparts. This is demonstrated in Fig. 5 and 6, which present, respectively, typical selected voltage profiles measured at various charge–discharge cycles from NCM-622 undoped (a) and zirconium doped (b) materials. These figures also show the cycling behavior of these electrodes at various current densities. We note that both Zr-doped and undoped materials show similar voltage profiles, as predicted by DFT calculations.

However, we have established that Zr-doped materials deliver slightly larger discharge capacities, especially at higher rates of 1C–4C, implying thus enhanced Li intercalation/deintercalation of these electrodes. The increased capacity of Zr doped NCM-622 could be attributed to the greater Ni^{2+}/Ni^{3+} ratio in this material compared to the undoped one, as discussed in the previous section. The positive effect of Zr-doping is confirmed by much lower polarization in discharge upon cycling, as shown in Fig. 5, and by obvious stabilization of the

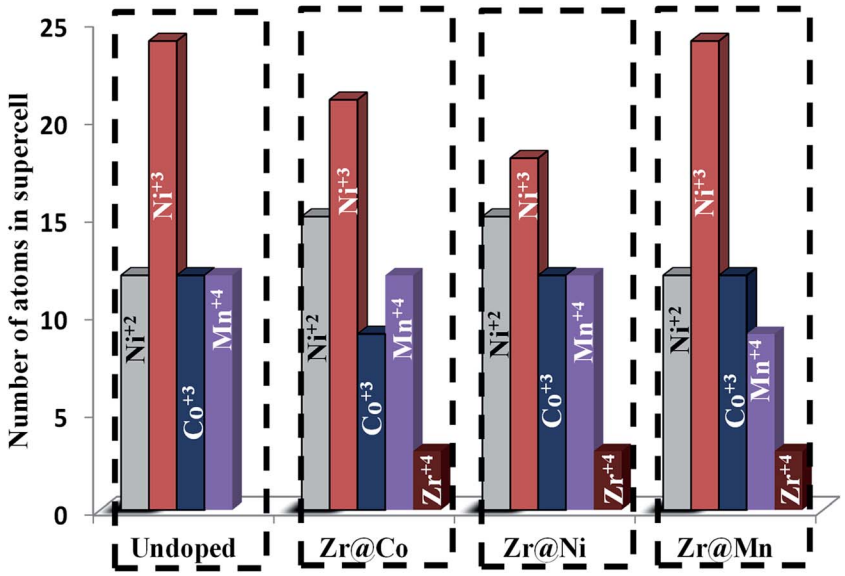

Fig. 3 Oxidation states of transition metals in undoped and NCM-622 with Zr doped at Ni, Co or Mn sites.

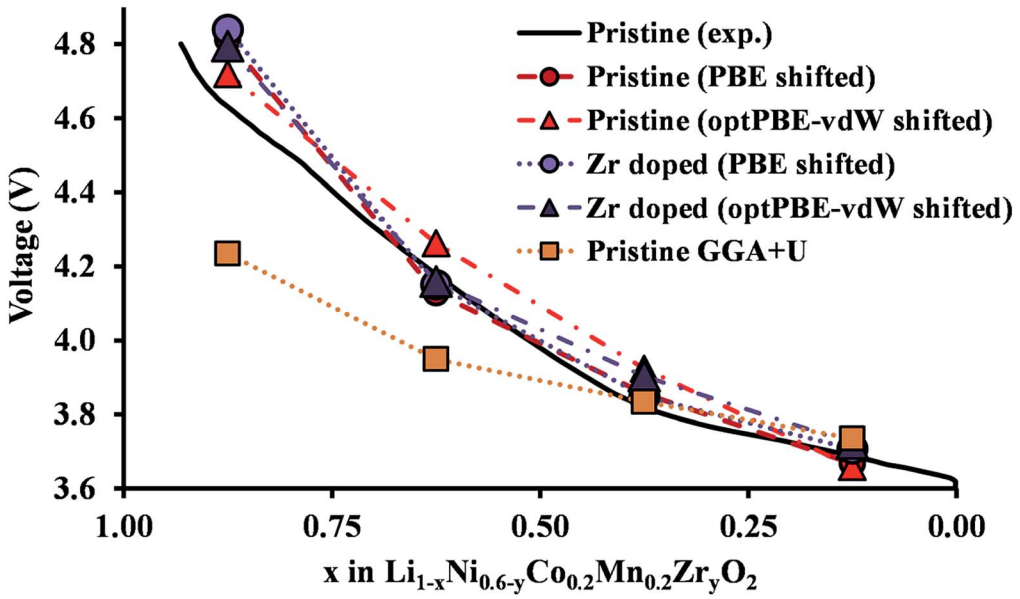

Fig. 4 Calculated and experimental voltage profiles for undoped and Zr-doped $Li_xNi_{0.6-y}Co_{0.2}Mn_{0.2}Zr_yO_2$ materials at different delithiation levels. The values of PBE and PBE with dispersion correction are rigidly shifted up by 0.9 eV and 0.6 eV, respectively. The black line represents the experimental voltage for $Li_xNi_{0.6}Co_{0.2}Mn_{0.2}O_2$ taken from ref. 47; $y = 0.00$ and $y = 0.05$ represent the undoped and doped systems, respectively. The experimental curve is plotted by considering a specific capacity of 250 mA h g^{-1} in the fully delithiated state.

mean voltage on discharge, as represented in the inset to Fig. 6. We demonstrate in Fig. 7, families of cyclic voltammograms measured with undoped and Zr-doped electrodes, (a) and (b), respectively, at a scan rate of 0.1 mV s^{-1} in the potential range of 2.8–4.3 V.

These results show that Zr-doped electrodes develop sharper anodic and cathodic voltammetric peaks, higher currents implying thus faster kinetics. They also reach stable quasi-equilibrium behavior even after the 1st cycle and demonstrate less charge over-potential for the subsequent CVs. In addition, Zr-doped $LiNi_{0.56}Co_{0.2}Mn_{0.2}Zr_{0.04}O_2$ electrodes exhibit much lower potential difference between anodic and cathodic voltammetric peaks, $\Delta E = E_a - E_c$ (compare the results shown in the insets to Fig. 7), indicating faster electrochemical kinetics both during the course of the first cycles and after 50 consecutive charge/discharge cycles. This was confirmed by the results of impedance measured from undoped and Zr-doped electrodes at various potentials during charge from 3.7 V to 4.3 V (Li-deintercalation), Fig. 8a–d. Much lower total impedance of $LiNi_{0.56}Co_{0.2}Mn_{0.2}Zr_{0.04}O_2$ electrodes, both after initial cycling

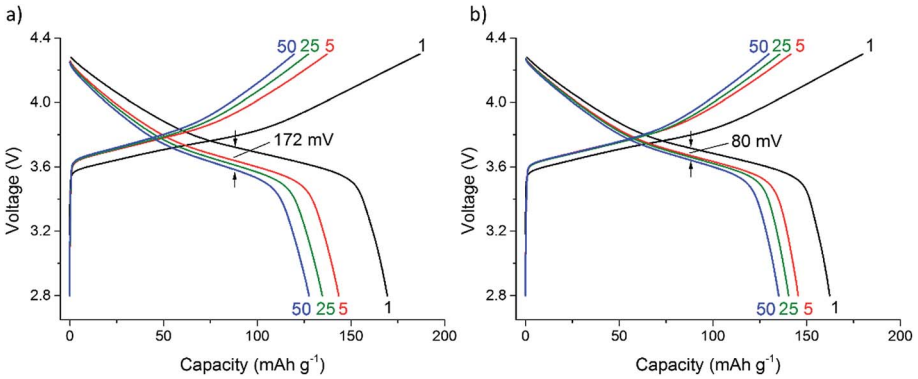

Fig. 5 Selected voltage profiles measured at 30 °C from electrodes comprising (a) undoped NCM-622 and (b) zirconium doped NCM-622 materials at the 1st cycle (C/15 rate, 10.6 mA h g^{-1}), and at 5th, 25th and 50th cycles (C/3 rate, 53.3 mA h g^{-1}). The irreversible capacity loss calculated from the first cycles is ~9% for the above electrodes.

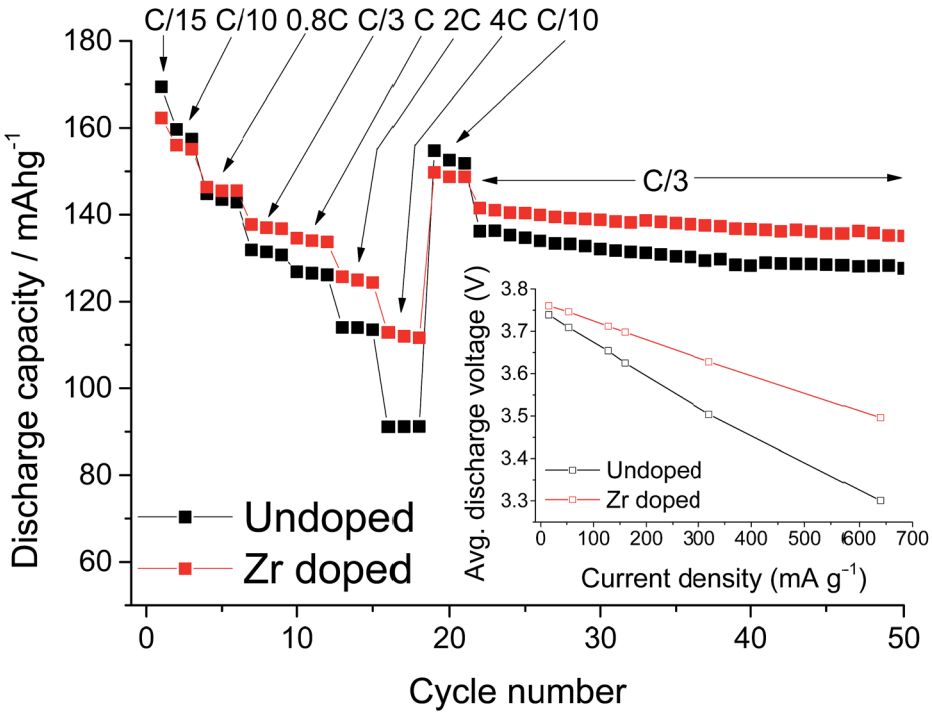

Fig. 6 Discharge capacity measured at various C rates (1C rate: 160 mA h g^{-1}) at 30 °C from electrodes comprising undoped NCM-622 and zirconium doped NCM-622 materials. These electrodes exhibited capacity retention of ~93 and ~96%, respectively, at a C/3 rate. The average discharge voltage as a function of the current density applied upon cycling of the above electrodes is shown in the inset.

at 30 °C and after 50 charge/discharge cycles at 45 °C, points to lower resistance of the Li^+ migration through surface films (R_{sf}) formed, as reflected in Fig. S9,† and to enhanced electrochemical charge-transfer reactions (Fig. S10†).

We also conclude from this figure that the charge-transfer resistance (R_{ct}) of Zr-doped electrodes remains unchanged upon Li^+ deintercalation and is constant during consecutive galvanostatic cycling at a moderate current density, in comparison to undoped electrodes. The lower resistances R_{sf} and R_{ct} of $LiNi_{0.56}Co_{0.2}Mn_{0.2}Zr_{0.04}O_2$ electrodes can be attributed to some extent to their modified and stable interface comprising the Zr^{4+}-enriched surface layer due to the dopant segregation and highly Li^+-conducting species with Zr–O bonds, like Li_2ZrO_3.[48] The latter were found to be present in the doped material as a minor phase detected by X-ray and electron diffraction studies. A similar phenomenon related to stabilization of the electrode/solution interface of doped cathode materials was also established in previous reports.[10,12,49] The modified interface of Zr-doped $LiNi_{0.56}Co_{0.2}Mn_{0.2}Zr_{0.04}O_2$ electrodes is reflected furthermore by the much lower total exothermic heat around 320 J g^{-1} of this material in reaction with an EC-EMC/$LiPF_6$ solution (as measured by differential-scanning calorimetry in a 190–400 °C range) compared to that of the undoped counterpart (~870 J g^{-1}). A detailed study of the thermal

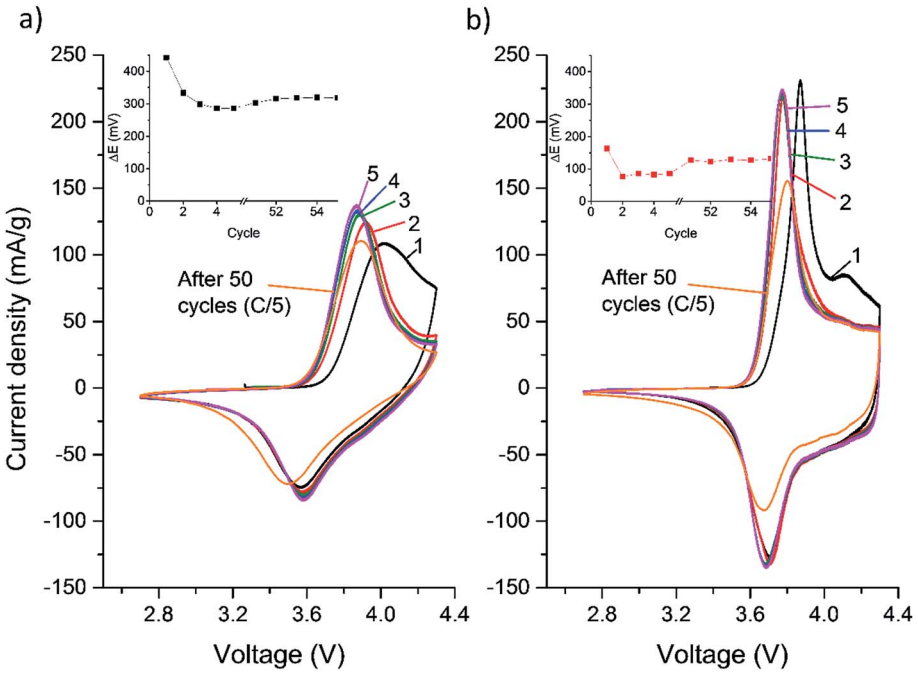

Fig. 7 Cyclic voltammograms (CVs) measured at 30 °C (scan rate 0.1 mV s^{-1}) from electrodes comprising (a) undoped NCM-622 and (b) zirconium doped NCM-622 materials. Shown are the initial five CVs (1–5, as indicated) and those measured after 50 consecutive galvanostatic cycles at a C/5 rate (45 °C). The insets to (a) and (b) demonstrate the potential difference $\Delta E = E_a - E_c$ of the anodic and cathodic voltammetric peaks measured as a function of cycles of undoped and Zr-doped electrodes, respectively.

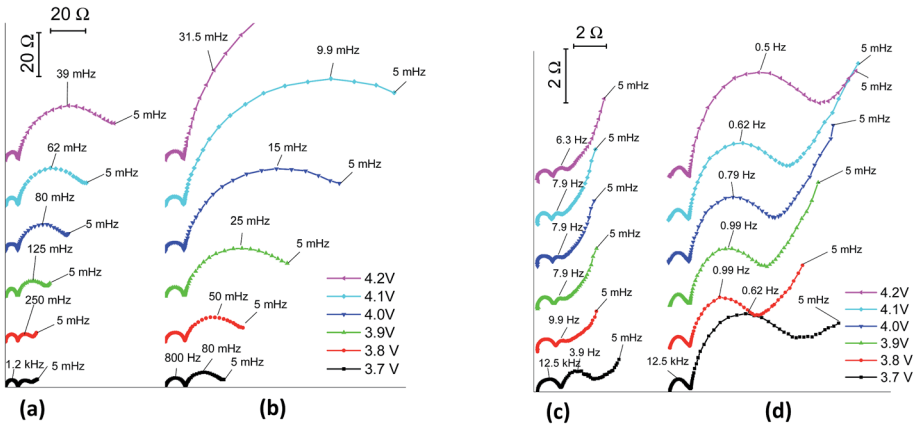

Fig. 8 Families of impedance spectra (Nyquist plots) measured at 30 °C at several potentials upon charge (Li^+-extraction) from electrodes comprising undoped NCM-622 and zirconium doped NCM-622 materials: (a) and (c) after 5 initial CVs and (b) and (d) after consecutive 50 galvanostatic cycles at a C/5 rate, at 45 °C, respectively. Selected frequencies are shown on the spectra. Note that the scale of charts (c) and (d) (Zr doped material) is smaller by an order of magnitude compared to that of charts (a) and (b) (undoped material).

behavior of the two materials in pristine and charged states will be reported in a separate paper from our groups. In the following section, we demonstrate by structurally sensitive X-ray and electron diffraction measurements how Zr-doping influences the structural stability of the layered oxide material subjected to electrochemical cycling.

Fig. 9 compares XRD profiles of undoped and doped pristine NCM-622 materials (black and blue colors, respectively), which were subjected to heat treatment at 900 °C for one hour. Also demonstrated in this figure are the XRD patterns obtained from these materials after electrochemical cycling (50 consecutive cycles at 45 °C) terminated by charge to 4.3 V.

All reflections in these patterns can be attributed to the rhombohedral ($R\bar{3}m$) Li(TM)O_2 phase, although overlapping peaks at 2θ = 38.5°, 44.7° and 65.1° also include Al_{111}, Al_{200} and Al_{220} peaks, respectively, that arise from the Al substrate. Due to the preferred orientation of the Al grains the reflection Al_{220} is rather strong, while the contribution of the peaks Al_{111} and Al_{200} is negligible.

Careful inspection of the diffraction patterns (Table S1†) reveals that the splitting of the (006)/(012) and (018)/(110) peaks

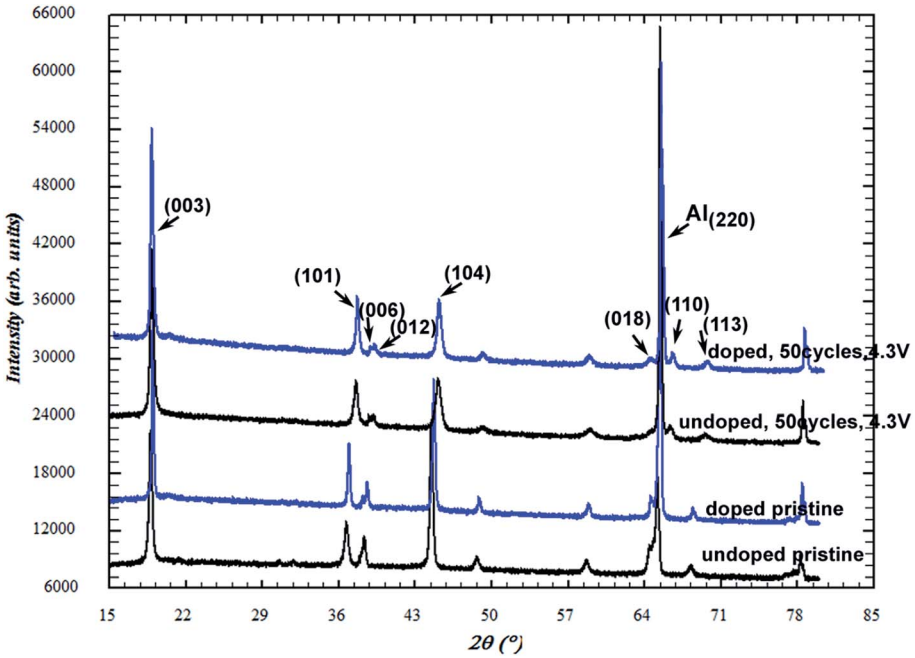

Fig. 9 XRD patterns measured from undoped $LiNi_{0.6}Co_{0.2}Mn_{0.2}O_2$ and Zr-doped pristine $LiNi_{0.56}Co_{0.2}Mn_{0.2}Zr_{0.04}O_2$ materials and from cycled electrodes (black and blue profiles, respectively). The strong peak at $2\theta = 65.1°$ arises from the Al-foil current collector.

remains after electrochemical cycling. Moreover, in the doped material, the splitting of the (018)/(110) peaks is noticeably greater. This indicates that hexagonal ordering persists suggesting that the cycled material still possesses a layered structure. Although XRD patterns from both undoped and doped cycled materials did not contain any indication of the structural transformation to the spinel phase, TEM examinations of some individual particles of undoped cycled material revealed, however, the presence of the spinel phase. Fig. 10 shows an example of the TEM image of the particle of the cycled material. The nano-beam electron diffraction (Fig. 10b) taken from the area marked "sp" on the periphery of the particle, which is outlined by a blue dashed line, clearly demonstrates that transformation from the layered to the spinel structure takes place, and the transition starts at the particle surface. The structure of the interior of the particle still remains rhombohedral, as illustrated by the corresponding indexed CBED diffraction shown in Fig. 10c.

Interestingly, analysis of the diffraction patterns of 15 cycled Zr-doped particles of this material did not reveal the presence of a spinel. All the particles were indexed in terms of the rhombohedral $R\bar{3}m$ phase (Fig. 11a and b).

It is noteworthy that the above mentioned presence of insignificant amount of the Li_2ZrO_3 phase in the doped material (demonstrated by XRD) was also detected in TEM. Among the CBED patterns recorded from the samples of doped material, some patterns could be uniquely indexed to the structure of Li_2ZrO_3, as demonstrated in Fig. 11c. Apparently, this phase, which appears in the material as a minor impurity, is formed while synthesizing the doped $Li_1Ni_{0.56}Zr_{0.04}Co_{0.2}Mn_{0.2}O_2$.

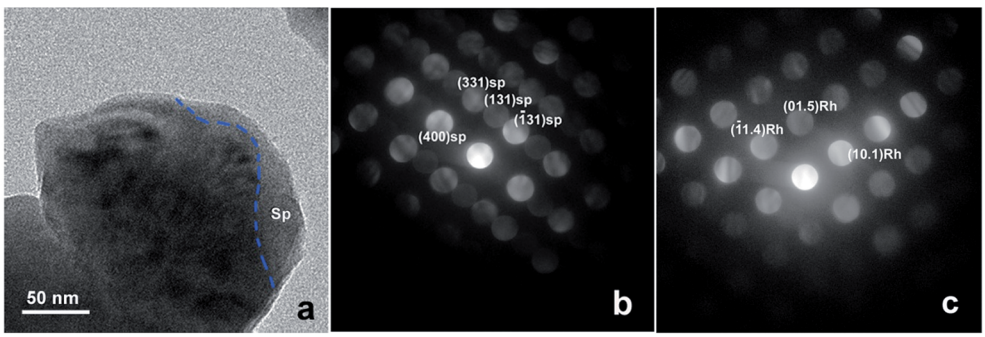

Fig. 10 TEM analysis of undoped $LiNi_{0.6}Co_{0.2}Mn_{0.2}O_2$ material subjected to 50 galvanostatic cycles at 45 °C: (a) TEM image of the individual particle; the blue line separates the original rhombohedral layered structure material from the material transformed to the cubic spinel; (b) CBED pattern from the area marked "sp"; (c) CBED pattern taken from the interior of the particle, which was indexed on the basis of the rhombohedral unit cell of $Li(TM)O_2$. Reflections of the rhombohedral phase are labeled as Rh.

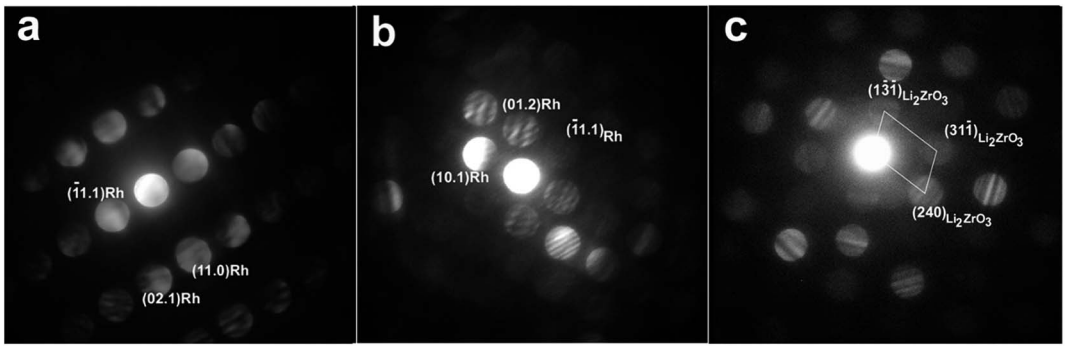

Fig. 11 The CBED patterns taken from the Zr-doped $LiNi_{0.56}Zr_{0.04}Co_{0.2}Mn_{0.2}O_2$ electrode material after 50 consecutive galvanostatic cycles at 45 °C. Patterns (a) and (b) were indexed on the basis of the unit cell of the rhombohedral (Rh) phase. The pattern in (c) shows the presence of Li_2ZrO_3 as a secondary phase from the self-combustion synthesis of the Zr-doped material.

3.4 Layered-to-spinel structural transformation

To understand why the Zr-doped samples do not show any layered to spinel transformation, we investigated the possible mechanism for such transformation in undoped and Zr-doped NCM-622. For transformation from a layered to a spinel structure to occur, 25% of the ions are required to migrate from the TM layer to the Li layer into adjacent octahedra.[50] Such layered-to-spinel transformations have been extensively studied in Li_x-MnO_2-based materials.[50,52] In the current case, Ni^{2+} migration is the most likely scenario leading to a layered-to-spinel transformation,[51,53] and hence we investigated the Ni^{2+} migration energy barriers in NCM-622. In particular, we computed diffusion paths from octahedral (O_h) sites (in the TM layer) to the corresponding tetrahedral (T_d) sites (adjacent to the Li layer). As the diffusion barriers are dependent on the Li-ion concentration,[54] we varied the number of Li vacancies to understand their effect on cation migration barriers. For instance, the Ni^{2+} migration barrier is high (>1 eV) in the case of two Li vacancies near the migrating Ni T_d site and a single Li vacancy at an adjacent octahedral site (Fig. 12a and d with Li present at encircled Li sites). Moreover, the T_d site is energetically less favorable compared to the O_h site. Interestingly, in the case of three Li vacancies (at lower lithium loading) near the migrating ion and one Li vacancy at the final migration site, the

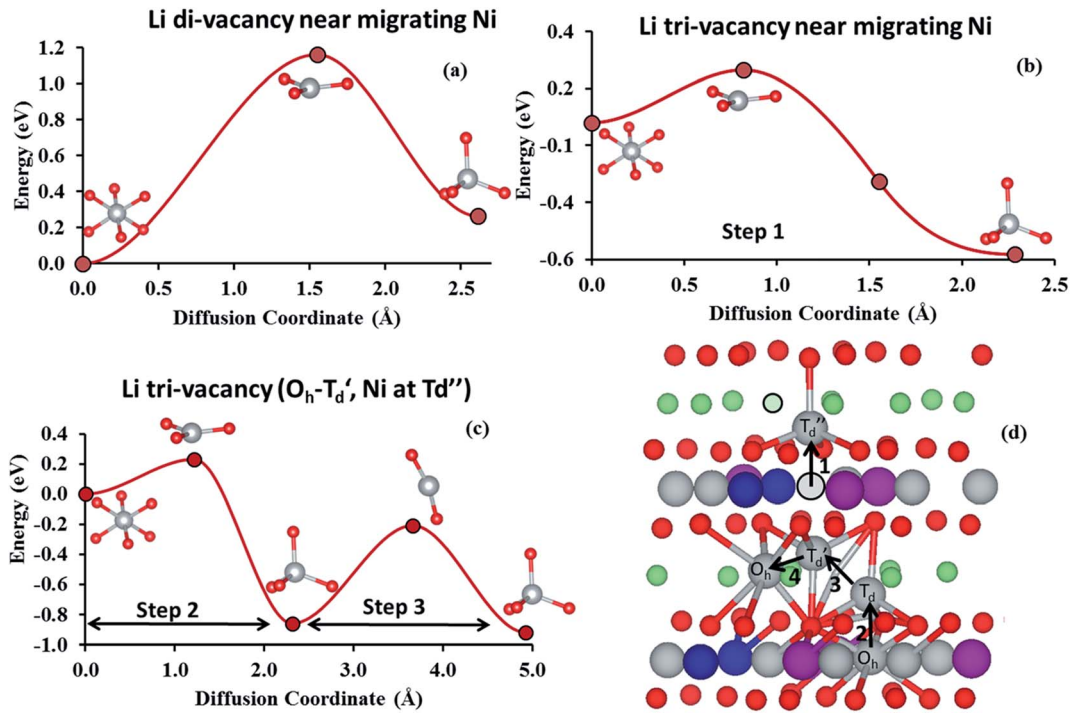

Fig. 12 Energy profiles for Ni migration obtained using PBE. O_h to T_d Ni migration barrier in undoped NCM-622 with Li (a) di-vacancy near a Ni T_d site and (b) tri-vacancy near the Ni T_d site. (c) O_h–T_d–T'_d Ni migration barrier in undoped NCM-622 with Li tri-vacancy with one Ni at the T''_d site (above the migrating ion layer). (d) Suggested mechanism for Ni^{2+} migration leading to a partial spinel nucleus. Color codes for spheres: red-oxygen atoms and grey-Ni atoms, violet-Mn atoms, blue-cobalt atoms.

Ni^{2+} migration barriers drop to 0.23 eV and the T_d site becomes significantly more stable compared to the corresponding O_h site (step 1, Fig. 12b and d with Li absent at the encircled Li sites). These results suggest rapid and irreversible Ni^{2+} ion migration upon lowering of the Li-ion concentration. It appears surprising that the T_d site becomes thermodynamically preferred over the O_h site, as the preliminary qualitative argument of crystal field stabilization energy suggests that Ni^{2+} has slight octahedral preference over tetrahedral sites. However, with four vacancies, $Ni(O)_6$ becomes distorted (Fig. S11b†) relative to the corresponding lithiated state (Fig. S11a†). This $Ni(O)_6$ asymmetry lowers the stability of the O_h site compare to the T_d site.

Based on the above results we may suggest the following mechanism: initially, Ni^{2+} from one TM layer rapidly migrates from an O_h to a corresponding T_d site (step 1, Fig. 12b), followed by an O_h to T_d migration of a second Ni^{2+} (in an adjacent layer) (step 2, Fig. 12c and d). This Ni can further migrate to a corresponding T'_d site (T_d–T'_d), with a somewhat higher barrier of ~0.7 eV (step 3, Fig. 12c and d). Since the stability of the T_d site is lower than that of the O_h site with lowering in the amount of Li vacancies, the last stage of Ni^{2+} migration from a T'_d site to an O_h site (in the Li layer) can be achieved by further cycling or *via* a Li concentration gradient, although this step was not modeled in the current study. Structures involved in this migration mechanism are shown in Fig. S12.†

To avoid layered-to-spinel transformations, one may dope the NCM lattice with a high-charge state cation, such as Zr^{4+}. NEB calculations show that the optimal Ni^{2+} migration paths do not involve T_d sites in the presence of Zr^{4+} in the lithium layer due to destabilization of the T_d sites due to strong electrostatic interaction with nearby Zr^{4+} ions. In the presence of Zr^{4+}, Ni^{2+} migration occurs *via* an O_h site (TM layer) to an O_h site (Li layer), involving a high-energy barrier of 1.52 eV (Li tri-vacancy) and 1.46 eV (Li tetra-vacancy). The high barrier is likely due to the involvement of an energetically unfavorable oxygen dumbbell transition state,[50,55] as well as repulsive electrostatic interaction with Zr^{4+}. Moreover, the presence of Zr^{4+} in the TM layer also destabilizes T''_d sites.

Hence, our computational results suggest that Ni^{2+} migration is hindered due to doping of Zr^{4+} at Ni sites near the dopants. A second important effect of the high charge state dopant is the reduction of the number of Ni^{3+} ions on doping, as these Jahn–Teller active ions (Ni^{3+}) could result in instability in the layered structure.

4. Conclusions

In this work, we presented a combined computational and experimental study aiming to understand the impact of high charge-state dopants, such as Zr^{4+}, on the structural stability and electrochemical behavior of the lithiated transition metal oxide $LiNi_{0.6}Co_{0.2}Mn_{0.2}O_2$. It was established that Zr-doped $LiNi_{0.6-x}Co_{0.2}Mn_{0.3}Zr_xO_2$ electrodes possess faster electrochemical kinetics, much lower surface film, and charge-transfer resistances measured from impedance spectra in the potential range of 3.7–4.3 V. These electrodes also exhibited higher discharge capacities during cycling at 45 °C, especially at high rates. An important finding of our work is that Zr-doped $LiNi_{0.6-x}Zr_xCo_{0.2}Mn_{0.3}O_2$ material retained its structure upon electrochemical cycling, in contrast to the undoped one, which underwent partial layered-to-spinel structural transformation, evidenced from analysis of nano-beam electron diffraction patterns.

Computational studies suggest that irreversible migration of Ni-ions in $LiNi_{0.6}Co_{0.2}Mn_{0.2}O_2$ upon the Li^+ deintercalation could result in partial structural layered-to-spinel transformation, hence explaining the experimentally observed change. Comparison of ion-diffusion paths in the undoped and doped materials presents a rational for how Zr can stabilize layered structures. In particular, we suggest that Zr plays a two-fold role in inhibiting the above transformation: destabilization of Ni tetrahedral sites and reducing the concentration of Jahn–Teller active Ni^{3+} ions. The current findings are expected to aid in the rational design of improved cathode materials for Li-ion batteries.

References

1 V. Etacheri, R. Marom, R. Elazari, G. Salitra and D. Aurbach, *Energy Environ. Sci.*, 2011, **4**, 3243–3262.
2 C. Masquelier and L. Croguennec, *Chem. Rev.*, 2013, **113**, 6552–6591.
3 M. S. Whittingham, *Chem. Rev.*, 2004, **104**, 4271–4302.
4 J. W. Fergus, *J. Power Sources*, 2010, **195**, 939–954.
5 Y. Zhang and C.-Y. Wang, *J. Electrochem. Soc.*, 2009, **156**, A527–A535.
6 M. Mladenov, R. Stoyanova, E. Zhecheva and S. Vassilev, *Electrochem. Commun.*, 2001, **3**, 410–416.
7 E.-S. Lee and A. Manthiram, *J. Mater. Chem. A*, 2013, **1**, 3118–3126.
8 Y.-S. He, L. Pei, X.-Z. Liao and Z.-F. Ma, *J. Fluorine Chem.*, 2007, **128**, 139–143.
9 L. Croguennec, J. Bains, M. Ménétrier, A. Flambard, E. Bekaert, C. Jordy, P. Biensan and C. Delmas, *J. Electrochem. Soc.*, 2009, **156**, A349–A355.
10 D. Aurbach, O. Srur-Lavi, C. Ghanty, M. Dixit, O. Haik, M. Talianker, Y. Grinblat, N. Leifer, R. Lavi, D. T. Major, G. Goobes, E. Zinigrad, E. M. Erickson, M. Kosa, B. Markovsky, J. Lampert, A. Volkov, J.-Y. Shin and A. Garsuch, *J. Electrochem. Soc.*, 2015, **162**, A1014–A1027.
11 Y. Koyama, H. Arai, I. Tanaka, Y. Uchimoto and Z. Ogumi, *J. Mater. Chem. A*, 2014, **2**, 11235–11245.
12 D. W. Shin, C. A. Bridges, A. Huq, M. P. Paranthaman and A. Manthiram, *Chem. Mater.*, 2012, **24**, 3720–3731.
13 J. Kim and K. Amine, *Electrochem. Commun.*, 2001, **3**, 52–55.
14 J. Kim and K. Amine, *J. Power Sources*, 2002, **104**, 33–39.
15 M. Guilmard, L. Croguennec and C. Delmas, *Chem. Mater.*, 2003, **15**, 4484–4493.
16 M. Guilmard, L. Croguennec, D. Denux and C. Delmas, *Chem. Mater.*, 2003, **15**, 4476–4483.
17 D. Aurbach, O. Srur-Lavi, C. Ghanty, M. Dixit, O. Haik, M. Talianker, Y. Grinblat, N. Leifer, R. Lavi and D. T. Major, *J. Electrochem. Soc.*, 2015, **162**, A1014–A1027.

18 L. Zhu, Y. Liu, W. Wu, X. Wu, W. Tang and Y. Wu, *J. Mater. Chem. A*, 2015, **3**, 15156–15162.
19 F. Wang, Z. Chang, X. Wang, Y. Wang, B. Chen, Y. Zhu and Y. Wu, *J. Mater. Chem. A*, 2015, **3**, 4840–4845.
20 S. H. Oh, S. M. Lee, W. I. Cho and B. W. Cho, *Electrochim. Acta*, 2006, **51**, 3637–3644.
21 H. J. Bang, B. C. Park, J. Prakash and Y. K. Sun, *J. Power Sources*, 2007, **174**, 565–568.
22 C. X. Ding, Y. C. Bai, X. Y. Feng and C. H. Chen, *Solid State Ionics*, 2011, **189**, 69–73.
23 S. Sivaprakash and S. Majumder, *J. Alloys Compd.*, 2009, **479**, 561–568.
24 G. Kresse and J. Hafner, *Phys. Rev. B: Condens. Matter Mater. Phys.*, 1993, **47**, 558–561.
25 G. Kresse and J. Hafner, *Phys. Rev. B: Condens. Matter Mater. Phys.*, 1994, **49**, 14251–14269.
26 G. Kresse and J. Furthmüller, *Comput. Mater. Sci.*, 1996, **6**, 15–50.
27 J. P. Perdew, K. Burke and M. Ernzerhof, *Phys. Rev. Lett.*, 1996, **77**, 3865–3868.
28 P. E. Blöchl, *Phys. Rev. B: Condens. Matter Mater. Phys.*, 1994, **50**, 17953–17979.
29 P. Xiao, Z. Deng, A. Manthiram and G. Henkelman, *J. Phys. Chem. C*, 2012, **116**, 23201–23204.
30 I. M. Markus, F. Lin, K. C. Kam, M. Asta and M. M. Doeff, *J. Phys. Chem. Lett.*, 2014, **5**, 3649–3655.
31 F. Zhou, M. Cococcioni, K. Kang and G. Ceder, *Electrochem. Commun.*, 2004, **6**, 1144–1148.
32 W. Luo and J. R. Dahn, *J. Electrochem. Soc.*, 2011, **158**, A110–A114.
33 J. Klimeš, D. R. Bowler and A. Michaelides, *Phys. Rev. B: Condens. Matter Mater. Phys.*, 2011, **83**, 195131.
34 K. Jiří, R. B. David and M. Angelos, *J. Phys.: Condens. Matter*, 2010, **22**, 022201.
35 G. Henkelman, B. P. Uberuaga and H. Jónsson, *J. Chem. Phys.*, 2000, **113**, 9901–9904.
36 S. P. Ong, V. L. Chevrier, G. Hautier, A. Jain, C. Moore, S. Kim, X. Ma and G. Ceder, *Energy Environ. Sci.*, 2011, **4**, 3680–3688.
37 L. S. Cahill, S. C. Yin, A. Samoson, I. Heinmaa, L. F. Nazar and G. R. Goward, *Chem. Mater.*, 2005, **17**, 6560–6566.
38 D. Zeng, J. Cabana, J. Bréger, W.-S. Yoon and C. P. Grey, *Chem. Mater.*, 2007, **19**, 6277–6289.
39 F. Weill, N. Tran, L. Croguennec and C. Delmas, *J. Power Sources*, 2007, **172**, 893–900.
40 Y. S. Meng, G. Ceder, C. P. Grey, W. S. Yoon, M. Jiang, J. Bréger and Y. Shao-Horn, *Chem. Mater.*, 2005, **17**, 2386–2394.
41 P. Strobel and B. Lambert-Andron, *J. Solid State Chem.*, 1988, **75**, 90–98.
42 J. M. Paulsen and J. R. Dahn, *J. Electrochem. Soc.*, 2000, **147**, 2478–2485.
43 M. Dixit, M. Kosa, O. S. Lavi, B. Markovsky, D. Aurbach and D. T. Major, *Phys. Chem. Chem. Phys.*, 2016, **18**, 6799–6812.
44 M. Labrini, F. Scheiba, A. Almaggoussi, M. Larzek, M. H. Braga, H. Ehrenberg and I. Saadoune, *Solid State Ionics*, 2016, **289**, 207–213.
45 G. G. Amatucci, J. M. Tarascon and L. C. Klein, *J. Electrochem. Soc.*, 1996, **143**, 1114–1123.
46 M. Aykol, S. Kim and C. Wolverton, *J. Phys. Chem. C*, 2015, **119**, 19053–19058.
47 Y. Wei, J. Zheng, S. Cui, X. Song, Y. Su, W. Deng, Z. Wu, X. Wang, W. Wang, M. Rao, Y. Lin, C. Wang, K. Amine and F. Pan, *J. Am. Chem. Soc.*, 2015, **137**, 8364–8367.
48 J. Ni, H. Zhou, J. Chen and X. Zhang, *Electrochim. Acta*, 2008, **53**, 3075–3083.
49 B. R. Long, M. K. Y. Chan, J. P. Greeley and A. A. Gewirth, *J. Phys. Chem. C*, 2011, **115**, 18916–18921.
50 J. Reed, G. Ceder and A. Van Der Ven, *Electrochem. Solid-State Lett.*, 2001, **4**, A78–A81.
51 J. Bréger, Y. S. Meng, Y. Hinuma, S. Kumar, K. Kang, Y. Shao-Horn, G. Ceder and C. P. Grey, *Chem. Mater.*, 2006, **18**, 4768–4781.
52 H. Kobayashi, Y. Arachi, H. Kageyama and K. Tatsumi, *J. Mater. Chem.*, 2004, **14**, 40–42.
53 S.-M. Bak, E. Hu, Y. Zhou, X. Yu, S. D. Senanayake, S.-J. Cho, K.-B. Kim, K. Y. Chung, X.-Q. Yang and K.-W. Nam, *ACS Appl. Mater. Interfaces*, 2014, **6**, 22594–22601.
54 M. Dixit, H. Engel, R. Eitan, D. Aurbach, M. D. Levi, M. Kosa and D. T. Major, *J. Phys. Chem. C*, 2015, **119**, 15801–15809.
55 A. Van der Ven, G. Ceder, M. Asta and P. D. Tepesch, *Phys. Rev. B: Condens. Matter Mater. Phys.*, 2001, **64**, 184307.

